Dalton Transactions

ROYAL SOCIETY OF CHEMISTRY

PAPER

View Article Online
View Journal | View Issue

Cite this: *Dalton Trans.*, 2026, **55**, 5529

Deciphering the mechanistic insights and reactivity trend of high-valent Mn/Fe/Co–oxo species toward C–H bond activation and oxygen atom transfer

Mukhtar Ahmed,[a] Manjeet Kumar,[b] Mursaleem Ansari,*[c] Manoj Kumar Gupta *[a] and Azaj Ansari *[a]

Understanding the structure and reaction pathways of high-valent metal–oxo species in C–H bond activation and oxygen atom transfer reactions is of great importance for improving their reactivity. Herein, we examine the reactivity of heme-based Mn/Fe/Co–oxo porphyrin complexes supported by an axial 1,3-dimethylimidazole ligand with substrates such as methane, 1,4-cyclohexadiene and dimethyl sulfide using density functional theory. Our calculations predicted quartet, triplet and doublet as the ground state for Mn, Fe and Co species, respectively. This study also reveals a reactivity trend of species Co > Fe > Mn during C–H bond activation and oxygen atom transfer reactions. Computed reaction profiles consistently identify the Co–oxo species as the most reactive, establishing the reactivity order. Furthermore, the formation of Co(III)-oxyl rather than a Co(IV)=O species in species **3** is supported by the pronounced spin density localized on the oxygen atom, orbital analysis, M–O bond length and stretching frequency trends. Non-covalent interactions and quantum theory of atoms in molecules analyses show stronger dispersive stabilization and greater Co–O bond polarization relative to the Mn and Fe analogues. Energy decomposition analysis further confirms more favorable interaction energies for the Co–O transition states. Our analysis demonstrates that the higher reactivity of species **3** arises from its uniquely polarized electronic structure, enhanced oxyl radical character, enhanced non-covalent transition state stabilization and stronger polarization in the Co–O bond. Overall, this work provides a new mechanistic understanding that moves beyond the traditional focus on the spin state and oxyl radical character and offers definitive design principles for developing bioinspired catalysts capable of selective C–H bond and oxygen atom transfer functionalization.

Received 29th December 2025,
Accepted 3rd March 2026

DOI: 10.1039/d5dt03104d

rsc.li/dalton

Introduction

High-valent metal–oxo species are widely recognized as important intermediates in oxidation reactions catalyzed by both metalloenzymes and synthetic metal complexes.[1] The chemistry of these reactive species, particularly for early transition metals, has been extensively explored,[1] owing to their stability imparted by vacant d-orbitals.[2] Numerous terminal oxo complexes of chromium,[3] manganese,[4] and iron[5,1e] have been synthesized, isolated, and comprehensively characterized. Their reactivity has been studied in depth, especially in the oxidation of organic substrates through processes such as oxygen atom transfer (OAT) and C–H bond activation.[6] OAT refers to reactions in which an oxygen atom is directly transferred from the metal–oxo unit to a substrate. Molecular models of heme and non-heme iron enzymes such as analogs of cytochrome P450 and other oxidative enzymes have been at the forefront of efforts to elucidate the mechanisms of OAT from iron–oxo complexes to organic substrates.[7] These studies have significantly advanced our understanding of how such species mediate various oxidation reactions.

High-valent manganese–oxo complexes coordinated by both heme and non-heme ligands have similarly attracted considerable attention in the fields of bioinorganic and oxidation chemistry. These species are postulated as crucial intermediates in manganese-catalyzed oxidation of organic substrates and in the water splitting process of Photosystem II.[8] Their efficient reactivity has led to numerous biomimetic investigations involving both OAT and C–H activation

[a]*Department of Chemistry, Central University of Haryana, Mahendergarh-123031, Haryana, India. E-mail: mkgupta@cuh.ac.in, ajaz.alam2@gmail.com*
[b]*Department of Chemistry, Indian Institute of Technology Bombay, Mumbai 400076, India*
[c]*Institut de Química Computacional i Catàlisi and Department of Chemistry, University of Girona, 17003 Girona, Spain. E-mail: mansaribhu@gmail.com*

reactions.[9,1f,h,6b] There is also sustained interest in the broader class of atom transfer reactions involving high valent metal–oxo complexes particularly those transferring oxygen, sulfur and nitrogen atoms due to their central role in various enzymatic systems. Examples include cytochrome P450, sulfite oxidase, phosphine oxidases, nitrate reductase, dimethyl sulfoxide (DMSO) reductase and oxygen evolution in Photosystem II.[10,9a,b] Given their biological and industrial significance, OAT reactions mediated by such high-valent species continue to be an active area of research.[11]

The iron(IV)–oxo porphyrin π-cation radical species (commonly referred to as Compound I) has long been recognized as a key oxidizing intermediate in cytochrome P450 catalysis responsible for both C–H activation and OAT reactions.[12,1c,f,2a,9d,9e] Its one-electron reduced form, the iron (IV)–oxo porphyrin complex (Compound II)[13] along with related non-heme iron(IV)–oxo analogs[14] also plays crucial roles in a wide range of oxidative transformations. Numerous studies have explored how the ligand environment influences the structure and reactivity of these complexes. Parameters such as electronic effects,[15] equatorial ring size,[16] ligand topology[17] and axial ligand identity[18] have been shown to profoundly affect their oxidative performance.

Similarly, mononuclear non-heme manganese complexes have demonstrated high catalytic activity in olefin epoxidation and alkane hydroxylation particularly when using environmentally benign oxidants like hydrogen peroxide in combination with carboxylic acids. These processes are often proposed to proceed *via* high-valent Mn(V)=O intermediates. Mn(V)–oxo species with macrocyclic ligands including porphyrins, corroles, corrolazines, and TAMLs have been synthesized and characterized by various spectroscopic and crystallographic methods.[19] Cobalt–oxo complexes have also emerged as promising oxidants with Co(IV)–oxo species suggested as key intermediates in cobalt mediated catalytic oxidations.[20] Building on these experimental findings, many research groups have developed biomimetic models that successfully mimic the reactivity of their enzymatic counterparts.[21] Computational studies have played a pivotal role in elucidating the electronic structures, bonding characteristics and reaction mechanisms of these high-valent metal–oxo complexes. These investigations have also helped decode the energetic profiles and kinetic pathways involved in both OAT and C–H activation.[22] Rajaraman and co-workers have provided mechanistic insights into the formation of Mn(III)=O and Mn(IV)=O with ligand $[H_3buea]^{3-}$ [H_3buea = tris[(*N-tert*-butylureaylato)-*N*-ethylene]aminato] using molecular oxygen under ambient conditions.[23] They also examined hydrogen atom transfer (HAT) from 9,10-dihydroanthracene (DHA) by these manganese–oxo complexes.[24] HAT refers to the abstraction of a hydrogen atom from a C–H bond by the metal–oxo species which results in the generation of a substrate radical and a metal-hydroxo intermediate. Likewise, de Visser and colleagues conducted theoretical studies on the activation of bisphenol A (BPA) *via* a model of human liver cytochrome P450.[25]

Furthermore, previous studies have demonstrated that incorporation of N-heterocyclic carbene donors into the porphyrinoid framework, by replacing the pyrrole group, leads to substantial changes in the electronic structure and coordination chemistry of iron complexes.[26] Inspired by these advancements, we have modeled terminal high-valent Fe, Mn and Co–oxo species supported by the dianion of 5,10,15,20-tetrakis(phenyl)porphyrin (TPP) and N-heterocyclic carbene (1,3-Me_2Imd) ligands based on Compound II-type intermediates (M(IV)=O).[27] These biomimetic systems are designed to investigate mechanistic pathways of C–H bond activation and OAT reactions involving substrates such as methane, 1,4-cyclohexadiene and dimethyl sulfide.[24] In previous studies, general reactivity patterns for various metal–oxo systems have been discussed;[5a,6e,9e,27j,28] however, a systematic and combined comparison of how the identity of the metal center controls mechanistic preferences and reactivity trends toward these reaction channels within an identical porphyrin framework remains limited. In this context, the present work aims to address this gap by employing a consistent computational framework to compare the reactivity of modeled high-valent Fe, Mn and Co–oxo porphyrin complexes toward these reactions. This study provides molecular level insight into the origin of metal dependent reactivity trends and explores the factors governing HAT and OAT pathways. Our objective is to evaluate the oxidative potential of these complexes and to elucidate the critical factors governing their reactivity toward C–H activation and OAT processes.

Computational details

The Gaussian16 program was used to perform all the DFT calculations.[29] A gas phase optimization was conducted without any constraints on local minima or transition states (TS). The calculations were performed using the dispersion-incorporated unrestricted hybrid density functional UB3LYP-D2.[30] For the transition metals, LANL2DZ (Los Alamos National Laboratory 2 Double-Zeta),[31] a commonly applied ECP type basis set was used. For the other organic elements (C, N, O and H), the 6-31G[32] basis set was employed. The "GEN" keyword was used for the generation of this mixed basis set. B3LYP-D2 has continuously shown during the course of its development and it is able to predict energetics and structures of transition metal-based catalytic reactions with high accuracy.[22b,c,27c,33] In order to promote smooth convergence, the fragmentation strategy[34] which is already included in Gaussian16 has also been used to increase the computing efficiency. Analytic frequency calculations were used to determine the transition state geometries that were optimized at the same theoretical level. Local minima have all the real frequencies, but only one imaginary frequency containing the appropriate vibrational distortion supported the transition state. Furthermore, a conductor-type polarized continuum model (CPCM)[35] was employed for single-point computations using a bigger (TZVP) basis set[36] in order to account for the solvent (acetonitrile) influence on all

of the optimized structures. The potential energy surface (PES) profile was estimated utilizing the solvation energies computed using the B3LYP-D2 method which incorporates free-energy corrections resulting from vibrational frequency computations. For the purpose of picture clarity, H atoms are removed from the optimized structures with the exception of the H atom included in transition state structures. Non-covalent interaction (NCI), electron localization function (ELF), localized orbital locator (LOL), interaction region indicator (IRI) and quantum theory of atoms in molecules (QTAIM) analyses are executed with the help of VMD 1.9.3 and Multiwfn 3.8 software.[37,38]

We applied energy decomposition analysis (EDA)[39] using the Gaussian16 program to investigate the factors contributing to barrier heights in the reaction. Specifically, this analysis was conducted on the H-atom abstraction step examining the associated barrier height ($\Delta E^{\ddagger}$).[40] This is defined as follows in eqn (1a) and (1b):

$$\Delta E^{\ddagger} = \Delta E_{\text{def}} + \Delta E_{\text{int}} \quad (1a)$$

where

$$\Delta E_{\text{def/dist}} = [\{E_{\text{R(TS)}} + E_{\text{S(TS)}}\} - \{E_{\text{R}} + E_{\text{S}}\}] \quad (1b)$$

The substrate and reactant equivalents are denoted by S and R in their structure of the transition state. Here, E_{S} and E_{R} are defined as the energy of the substrate and reactant in their undistorted state, whereas $E_{\text{S(TS)}}$ and $E_{\text{R(TS)}}$ are the single-point energy of the separated substrate and oxidant fragments in the transition state.

The total deformation energy (ΔE_{def}) represents the energy needed to distort both the substrate and the oxidant into their geometries in the transition state (TS). The interaction energy (ΔE_{int}) is the energy between these deformed reactants as they are brought to their TS distances. Interaction energy (1c) can be stabilizing ($\Delta E_{\text{int}} < 0$) when the orbital mixing term (ΔE_{orb}) is dominant and there is a favorable electrostatic interaction (ΔE_{el}). Alternatively, ΔE_{int} may be destabilizing ($\Delta E_{\text{int}} > 0$) due to steric repulsions denoted in eqn (1c) as $\Delta E_{\text{Pauli(steric)}}$.[41]

$$\Delta E_{\text{int}} = \Delta E_{\text{orb}} + \Delta E_{\text{el}} + \Delta E_{\text{Pauli(steric)}} \quad (1c)$$

Here, we used notations $^{\text{M}}\text{A–X}_{\text{N}}$ where the superscript 'M' denotes the spin multiplicity and the subscript N denotes the different spin configurations (high spin, low spin *etc.*) of the Mn/Fe/Co species. A and X represent the name and number of complexes.

Results and discussion

This report presents a detailed analysis of three modeled high-valent manganese–oxo (species **1**), iron–oxo (species **2**) and cobalt–oxo (species **3**) catalytic systems denoted as $\text{M}^{n+}\text{O(TPP)(Im)}$ (M^{n+} = Mn^{IV}, Fe^{IV}, Co^{IV}; TPP = *meso*-tetraphenylporphyrin; Im = 1,3-Me_2Imd). The study primarily focuses on investigating the geometry, spin-state energetics, electronic structures and mechanistic behavior of these systems. All the possible spin states are considered to comprehensively explore the reaction mechanisms. To evaluate the catalytic performance, substrates such as methane (CH_4), cyclohexadiene (CHD) and dimethyl sulfide (SMe_2) are employed as they are widely utilized in studies of C–H bond activation and oxygen atom transfer reactions. The subsequent sections delve into the electronic structure of these species and then in-depth examination of their catalytic capabilities in C–H bond activation and oxygen atom transfer reactions followed by comparative analysis.

Electronic structure and spin-state energetics of species 1–3

All three species have 1,3-Me_2Imd carbene as a supporting ligand to the M–O (M=Mn/Fe/Co) axis whereas the TPP ligand is perpendicular to the M–O axis (see Scheme S1of the SI). We have optimized possible spin surfaces of species **1–3** and the optimized geometry of the ground state with key geometric parameters are shown in Fig. 1. DFT calculations reveal that species **1** (Fig. 1(a)) has a quartet (^{4}**R-1$_{\text{hs}}$**) as the ground state while the doublet state (^{2}**R-1$_{\text{ls}}$**) lies at 51.0 kJ mol^{-1} higher in energy (see Table S1 of the SI). Similarly, species **2** has a triplet (^{3}**R-2$_{\text{is}}$**) as the ground state (Fig. 1(c)) while species **3** has doublet (^{2}**R-3$_{\text{ls}}$**) as the ground state (Fig. 1(e)). All the computed ground states are consistent with the earlier reports.[42,26c] The singlet (^{1}**R-2$_{\text{ls}}$**) and quintet (^{5}**R-2$_{\text{hs}}$**) spin states of species **2** lie at 125.0 and 52.9 kJ mol^{-1} higher in energy while the quartet (^{4}**R-3$_{\text{is}}$**) and sextet (^{6}**R-3$_{\text{hs}}$**) spin states of species **3** lie at 59.3 and 123.2 kJ mol^{-1}, respectively (see Tables S2 and S3 of the SI).

In the previous study, DLPNO-CCSD(T) calculations identified the triplet and doublet states as the respective ground states of species **2** and **3**.[42] These findings are consistent with the DFT results which further support the reliability of the employed methodology.[33c,43] The Mn–O bond length of species **1** is computed to be 1.686 Å for the quartet and 1.707 Å for the doublet spin states. Similarly, the Fe–O bond length of species **2** is computed to be 1.671 Å (singlet), 1.672 Å (triplet) and 1.662 Å (quintet), whereas 1.854 Å (doublet), 1.699 Å (quartet) and 1.924 Å (sextet) in the case of Co–O. These computed bond parameters of all the three species are

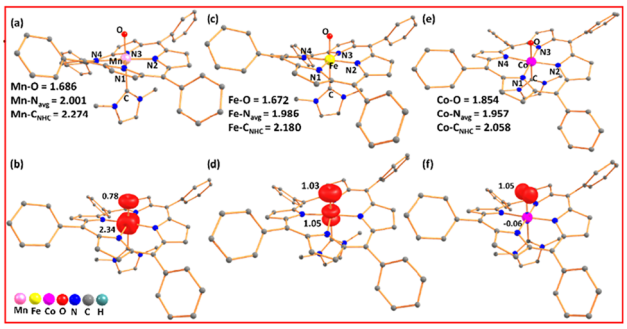

Fig. 1 Optimized structures along with the corresponding spin density plots of (a and b) ^{4}**R-1**, (c and d) ^{3}**R-2** and (e and f) ^{2}**R-3** (contour value = 0.03) (given bond lengths are in Å).

in agreement with slightly different ligand architectures (see Tables S4–S6 of the SI).[43a,44] The computed spin density values at Mn, Fe and Co centres of species **1–3** are found to be 2.34, 1.05 and −0.06, respectively (Fig. 1(b, d and f) and Tables S7–S9 of the SI). Furthermore, the computed spin density (ρ) at the oxygen atom is found to be 0.78, 1.03 and 1.05 for species **1**, **2** and **3**, respectively. A significant spin density is found to be at the oxygen centre of species **1–3** (see Fig. 1(b, d and f) and Tables S7–S9 of the SI) which can facilitate the catalytic activity toward C–H bond activation and oxygen atom transfer reactions.[45]

Furthermore, the electronic configuration for the ground state of species **1** and species **2** is found to be $(d_{xy})^1(d_{xz})^1(d_{yz})^1(d_{x^2-y^2})^0(d_{z^2})^0$ and $(d_{xy})^2(d_{xz})^1(d_{yz})^1(d_{x^2-y^2})^0(d_{z^2})^0$, whereas it is $(\delta_{xy})^2(\pi_{xz})^2(\pi_{yz})^2(\delta_{x^2-y^2})^0$ $(\sigma_{z^2})^0(\sigma O_{pz})^2(\pi^* O_{py})^2(\pi^* O_{px})^1$ for species **3** (see Fig. S1–S3 of the SI). The electronic configuration of species **3** is different from that of species **1** and **2** because of low-lying d-orbitals of cobalt.[42,46] The bonding π(Co–O) orbitals arise primarily from the Co based d-orbital, whereas the corresponding antibonding π*(Co–O) orbitals are dominated by O-based p-orbitals. This electronic distribution suggests that the bonding in the doublet state of species **3** is more appropriately described as a Co(III) center bound to an oxyl radical ($O^{\bullet -}$) with the unpaired electron residing in a p orbital oriented perpendicular to the Co–O bond axis (Fig. S3 of the SI).[46]

Molecular electrostatic potential (MEP) surfaces are computed to gain further insight into charge distribution in species **1–3** (Fig. S4 of the SI). In all three species, the oxygen centre is located in the most negative potential region (red) which highlights its electron-rich nature, making it susceptible for electrophilic attack.[47] The relationship between the M–O bond length (Å) and the corresponding stretching frequency was further examined using Badger's rule.[48] A near-linear correlation was observed when plotting the calculated bond lengths against $1/\nu^{2/3}{}_{M-O}$ ($cm^{2/3}$) as shown in Fig. 2 (R^2 = 0.98).[49] This strong correlation demonstrates that Badger's rule is also applicable to the computed high-valent Mn, Fe and Co–oxo porphyrin species. From this plot, it is concluded that the bond length variation in M–O affirms that the species **1** and species **2** are the true Mn/Fe(IV)–oxo units, whereas the species **3** is the Co(III)–oxyl unit. The data validate the expected inverse correlation between bond strength and bond length as per Badger's rule.[49]

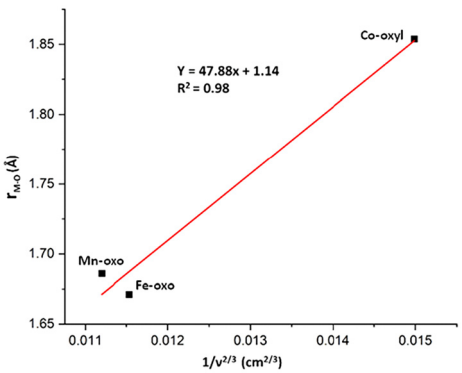

Fig. 2 Badger plot for the M–O bond length of species **1–3** *versus* $1/\nu^{2/3}{}_{M-O}$ ($cm^{2/3}$) with the ν_{M-O} stretching vibration for the M–O bond.

Reactivity of 1–3 towards methane

The adopted mechanism for methane hydroxylation by species **1–3** is shown in Scheme S1 of the SI. This generic mechanism involves the CH_4 substrate approaching the metal–oxo (R) centres to form a reactant complex (RC) adduct. After the formation of the adduct, species **1–3** activate the C–H bond of CH_4 in the first step *via* **TS1** leading to the formation of a metal-hydroxo (M–OH) along with the CH_3 radical (**INT1**). In the subsequent step, –OH rebound *via* **TS2** leading to a hydroxylated product (**INT2**) which further leads to the formation of the M(II) precursor. This proposed mechanism is consistent with previous studies on related complexes.[50,4b,6a,1f,41a] To gain a deeper insight into the reactivity pattern of the three complexes, we computed the activation barriers for C–H bond activation of a methane molecule.

For the species **1**, the computed potential energy (PESs) diagram is shown in Fig. 3. Here, the quartet (^{4}**R-1$_{hs}$**) spin surface is found as the ground state and a reactant complex (^{4}**RC-1$_{hs}$**) is formed upon approaching CH_4 which is lying at 23.0 kJ mol$^-$ relative to the reactant while its doublet spin surface (^{2}**RC-1$_{ls}$**) is found at 71.5 kJ mol^{-1} which reflects that the reaction will proceed *via* ^{4}**RC-1$_{hs}$**. In the next step, the reactant complex (^{4}**RC-1$_{hs}$**) abstracts the hydrogen leading to the formation of the first transition state (^{4,2}**TS1-1**) which requires 102.2 kJ mol^{-1} and 156.4 kJ mol^{-1} at the quartet (^{4}**TS1-1$_{hs}$**) and the doublet surfaces (^{2}**TS1-1$_{ls}$**) indicating that the hydrogen abstraction takes place at the high spin surface. The computed Mn–O (1.838 Å) and O···H (1.122 Å) bond lengths of the

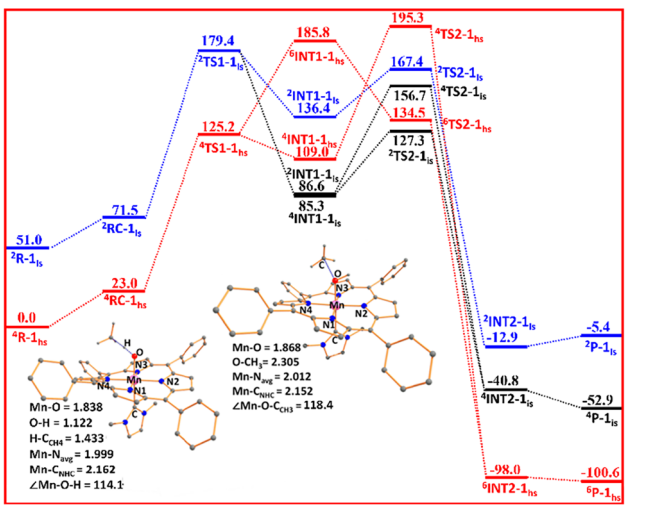

Fig. 3 The key geometric parameters of the transition states (^{4}**TS1-1$_{hs}$** and ^{2}**TS2-1$_{ls}$**) and energy profile (ΔG in kJ mol^{-1}) for C–H bond activation of CH_4 by **1** (given bond lengths and bond angles are in Å and °).

^{4}**TS1-1$_{hs}$** confirm the formation of the transition state, whereas the Mn–O–H angle is computed to be 114.1° suggesting the π-pathway. In ^{4}**TS1-1$_{hs}$**, the spin density on the Mn and O centres is found to be 2.00 and 0.51, respectively, whereas C of methane possessing a significant spin density of 0.70 suggests the formation of a radical rather than the cationic or anionic character (see Table S7 of the SI). Following hydrogen atom abstraction, the intermediate **INT1-1** is formed. Here, we have computed all possible interactions of the intermediate (Mn(III)–OH) with the methyl radical (*i.e.*, all possible interactions are summarized in Table S10 of the SI).[51] Computed results show that ^{4}**INT1-1$_{is}$** is located at 85.3 kJ mol^{-} while the other spin surfaces are found at higher energy (see Fig. 3 and Table S10 of the SI). Subsequently, the reaction then proceeds through a second transition state (**TS2-1**; see Table S11 of the SI). Among all the computed spin states of **TS2-1**, the intermediate spin state (^{2}**TS2-1$_{is}$**) shows a lower energy barrier (42.0 kJ mol^{-1}) compared to the other spin states such as high spin (^{6,4}**TS2-1**) (49.2 and 110.0 kJ mol^{-1} for ^{6}**TS2-1$_{hs}$** and ^{4}**TS2-1$_{hs}$**), intermediate spin (71.4 kJ mol^{-1} for ^{4}**TS2-1$_{is}$**) and low spin (82.1 kJ mol^{-1} for ^{2}**TS2-1$_{ls}$**) surfaces. In the ^{2}**TS2-1$_{is}$** transition state, the Mn–O bond undergoes further elongation (1.868 Å), while a new O···C bond (2.305 Å) is simultaneously formed (Fig. 3 and Table S4 of the SI). The bond angle of Mn–O–C and Mn–O–H is found to be 118.4° and 113.6°, respectively, which also indicate the π-pathway. Notably, the energy of ^{2}**TS2-1$_{is}$** is lower than that of ^{4}**TS1-1$_{hs}$**, suggesting that the HAT step is the rate-determining step rather than the rebound step. This transition state leads to the formation of **INT2-1** stabilized at −98.0 kJ mol^{-1} at ^{6}**INT2-1$_{hs}$** (see Fig. 3 for other states). In the last step, the –OH group is expected to rebound to the methyl radical to give methanol and the product which is further stabilized at −100.6 kJ mol^{-1} (^{6}**P-1$_{hs}$**, see Fig. 3 for other states). Our DFT computed results are consistent with the previous report for high-valent transition metal–oxo systems towards C–H activation.[52]

Similarly, we have computed the energy profile for the C–H bond activation of methane by species **2** and is shown in Fig. S5 of the SI. For species **2**, ^{3}**R-2$_{is}$** is found as the ground state followed by ^{5}**R-2$_{hs}$** (52.9 kJ mol^{-1}) and ^{1}**R-2$_{ls}$** (125.0 kJ mol^{-1}) states.

The computed barrier height for the hydrogen atom abstraction is estimated to be 80.6 kJ mol^{-1} (^{3}**TS1-2$_{is}$**) followed by ^{5}**TS1-2$_{hs}$** (143.8 kJ mol^{-1}) and ^{1}**TS1-2$_{ls}$** (176.2 kJ mol^{-1}) (see Fig. S5 of the SI). The Fe–O–H bond angle is 112.4° depicting the π-channel (see Table S5 of the SI). The Mulliken spin density values are found to be 0.91 and 0.55 at the Fe and O centre, while 0.76 at the carbon of CH_3 suggests the formation of radical character (see Table S8 of the SI). In the next step, formation of Fe(III)–OH along with the methyl radical intermediate takes place with ^{3}**INT1-2$_{ls}$** at 56.2 kJ mol^{-1} (see Table S10 of the SI for other states). The rebound barrier for this state is 32.6 kJ mol^{-1} (^{3}**TS2-2$_{ls}$**) (see Fig. S5 and Table S11 of the SI). Here also, the HAT step is the rate-determining step over OAT. This transition state leads to the formation of ^{5,3,1}**INT2-2** where ^{1}**INT2-2$_{ls}$** is stabilized at −98.9 and the final product complex ^{5}**P-2$_{hs}$** is further stabilized at −99.5 kJ mol^{-1} (see Fig. S5 for other states).

Furthermore, the PESs for the C–H bond activation of methane by the species **3** are also computed and ^{2}**R-3$_{ls}$** is found as the ground state (Fig. S6 of the SI). The calculated possible spin states of the reactant complex show that ^{2}**RC-3$_{ls}$** (10.3 kJ mol^{-1}) is the ground state. The computed barrier for abstraction of hydrogen is 23.6 kJ mol^{-1} for the ^{2}**TS1-3$_{ls}$** (see Fig. S6 for the other states). The computed bond lengths of the ^{2}**TS1-3$_{ls}$** also depict the formation of the transition state (see Fig. S6 and Table S6 of the SI). This hydrogen atom abstraction step yields the radical-type intermediate where ^{2}**INT1-3$_{ls}$** (−3.5 kJ mol^{-1}) is found as the ground state (see Table S10 of the SI). In the next step, the oxygen transfer takes place *via* ^{2}**TS2-3$_{ls}$** and the estimated barrier is found to be 35.2 kJ mol^{-1} (see Fig. S6 and Table S11 for other states). In the next step, ^{2}**INT2-3$_{ls}$** and ^{4}**INT2-3$_{hs}$** are formed and are thermodynamically stabilized at −148.8 and −136.6 kJ mol^{-1}, respectively. The formation of the product is further stabilized at −167.1 kJ mol^{-1} (^{2}**P-3$_{ls}$**) indicating the facile formation as compared to the species **1** and **2**. Notably, the low-spin surface offers a lower-energy pathway throughout the transformation compared to both the intermediate and high-spin states. The spin density value of Co (−0.02) and O (0.45) for ^{2}**TS1-3$_{ls}$** shows the spin delocalization between cobalt and oxygen centres which leads to hydrogen abstraction and consistent with a radical-type transition state. As shown in Fig. 4, it is concluded that the overall calculated barrier height shows that species **3** is more reactive than the species **1** and **2** and these results are consistent with the previous study.[53]

Reactivity of 1–3 towards cyclohexadiene

Furthermore, we have also tested the reactivity trend of species **1–3** toward C–H activation of cyclohexadiene (CHD) (see Scheme S2 of the SI) and the computed energy profile for CHD activation by species **1–3** is shown in Fig. S7–S9 of the SI. It

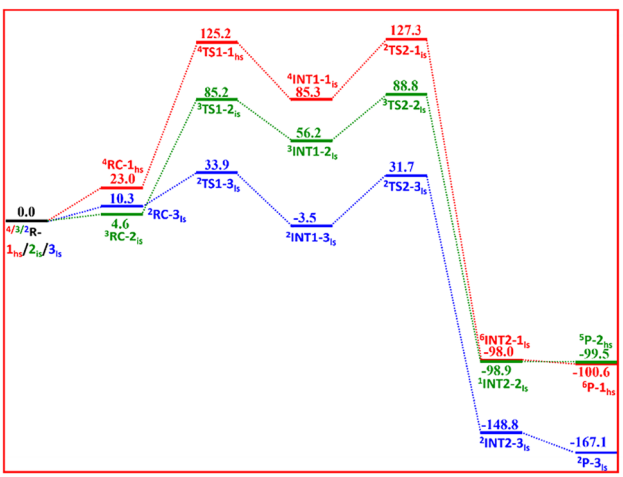

Fig. 4 Computed potential energy (Δ*G* in kJ mol^{-1}) surface of ground states for methane hydroxylation by **1** (red), **2** (green) and **3** (blue).

demonstrates a stepwise mechanism that proceeds *via* two transition states (**TS1** and **TS2**) which involves sequential abstraction of two allylic hydrogen atoms (Scheme S2 of the SI).[54] Here, the computed spin state of the reactant complex shows ^{4}**RC-1$_{hs}$** as the ground state which is lying at 18.0 kJ mol^{-1} from the ^{4}**R-1$_{hs}$**. Furthermore, the estimated barrier for first hydrogen abstraction of CHD is found to be 26.1 kJ mol^{-1} at the high-spin surface (^{4}**TS1-1$_{hs}$**) while 37.4 kJ mol^{-1} at the low spin (^{2}**TS1-1$_{ls}$**) (see Fig. S7 of the SI for other states). In the optimized geometry of ^{4}**TS1-1$_{hs}$**, Mn–O, C···H and O···H bond lengths are computed to be 1.770, 1.327 and 1.236 Å, whereas the Mn–O–H bond is found to be 120.0° which indicates the π-pathway (see Table S4 in the SI). The spin density values of 0.54 (oxygen) and 0.31 (carbon) depict the formation of oxyl character at the oxo centre and radical character at the carbon of CHD (see Table S7 in the SI). This step results in the formation of intermediate ^{4}**INT1-1$_{is}$** which lies at −69.7 kJ mol^{-1} below the reactant, highlighting the thermodynamic driving force associated with the more stabilized allylic radical (see Table S10 of the SI). In the next step, Mn(III-OH) interacts with the monohydrohexadiene radical (MHD) and abstracts the second hydrogen, resulting in benzene as a product. Here, all the possible spin surfaces for **TS2** are computed (see Fig. S7 and Table S11 of the SI).[51] The computed barrier for the second hydrogen abstraction is 26.8 kJ mol^{-1} (^{2}**TS2-1$_{is}$**). Both the transition states involve Mn=O···H–C interactions consistent with sequential hydrogen atom abstraction steps rather than rebound-type recombination. The intermediate formed after the second hydrogen atom abstraction stabilized at −256.9 kJ mol^{-1} (^{6}**INT2-1$_{hs}$**) which further converted into the final product at −292.3 kJ mol^{-1} on the high spin surface (^{6}**P-1$_{hs}$**) (see Fig. S7 for other states). These large negative values reflect the formation of a highly stabilized conjugated diene and Mn(II)–OH$_2$ species.

Similarly, for species **2**, the PESs (Fig. S8 of the SI) show that the intermediate-spin reactant complex (^{3}**RC-2$_{is}$**) is the ground state (−12.4 kJ mol^{-1}). The first hydrogen abstraction proceeds *via* ^{3}**TS1-2$_{is}$** with a barrier of 28.6 kJ mol^{-1} (see Fig. S8 for other states). A spin density value of 0.33 on the substrate carbon confirms the radical character (see Table S8 of the SI). The resulting Fe(III)–OH/MHD radical intermediate (**INT1-2**) has a triplet ground state (^{3}**INT1-2$_{ls}$**) lying at −101.1 kJ mol^{-1} (see Fig. S8 and Table S10 of the SI for other spin states). Subsequently, the second hydrogen abstraction occurs *via* **TS2** with a 25.4 kJ mol^{-1} barrier (^{1}**TS2-2$_{ls}$**) (see Fig. S8 and Table S11 for other spin states). The corresponding intermediate (^{1}**INT2-2$_{ls}$**) is stabilized at −294.3 kJ mol^{-1} and the final product (^{5}**P-2$_{hs}$**) is strongly exergonic at −306.6 kJ mol^{-1} (see Fig. S8 for other states). Overall, the first hydrogen abstraction is the rate-determining step consistent with the known behavior of Fe-porphyrin systems in hydrocarbon oxidation.[55]

For species **3**, the PESs for C–H bond activation of CHD are illustrated in Fig. S9 of the SI. The reaction starts from the doublet ground state (^{2}**R-3$_{ls}$**) forming the reactant complex ^{2}**RC-3$_{ls}$** at −29.8 kJ mol^{-1}. The first hydrogen atom abstraction occurs *via* ^{2}**TS1-3$_{ls}$** with a remarkably low barrier of 7.7 kJ mol^{-1} indicating low kinetic barrier and high exergonicity (see Fig. S9 of the SI for other states). Thus, species **3** exhibits a significantly lower first hydrogen atom abstraction barrier compared to species **1** and **2**. The ^{2}**TS1-3$_{ls}$** transition state features an elongated Co–O bond (1.869 Å) and a forming O···H bond (1.347 Å) with a Co–O–H bond angle of 114.4°. The resulting intermediate ^{2}**INT1-3$_{ls}$** is stabilized at −159.9 kJ mol^{-1} reflecting the strong thermodynamic favorability of CHD radical formation which is more stable than the methyl radical observed in methane oxidation (see Fig. S9 and Table S10 of the SI). The second hydrogen atom abstraction proceeds *via* ^{2}**TS2-3$_{ls}$** with a 33.3 kJ mol^{-1} barrier forming a doublet intermediate ^{2}**INT2-3$_{ls}$** which is stabilized at −345.1 kJ mol^{-1} (see Fig. S9 and Table S11 of the SI for the other spin states). In the next step, product complex ^{2}**P-3$_{ls}$** is stabilized at −361.2 kJ mol^{-1}. Overall, the computed energy profile (see Fig. 5.) predicts that CHD oxidation by species **3** can be more favorable on the low-spin doublet surface which can further depict the higher reactivity of the Co–oxo species.

Reactivity of 1–3 towards dimethylsulfide

To further elucidate the oxidative capabilities of species **1–3**, we examined the sulfur oxidation reaction using dimethylsulfide as the substrate and evaluated the kinetic requirements of this oxidation reaction. In contrast to the stepwise mechanism adopted for C–H activation of substrates such as CH_4 and CHD, the oxidation of dimethyl sulfide (SMe_2) proceeds *via* a direct OAT mechanism (see Scheme S3 in the SI). Here, we have calculated the energy profile (see Fig. 6 and S10–S12 of the SI) for species **1–3** which reveals the formation of a transition state through which the terminal oxo ligand is transferred to the sulfur centre of SMe_2. The initial association of the species **1–3** with SMe_2 forms a reactant complex where the quartet (^{4}**RC-1$_{hs}$**), triplet (^{3}**RC-2$_{is}$**) and doublet (^{2}**RC-3$_{ls}$**) spin states are found to be ground states for species **1–3**, respectively. The OAT reaction proceeds *via* concerted transition states

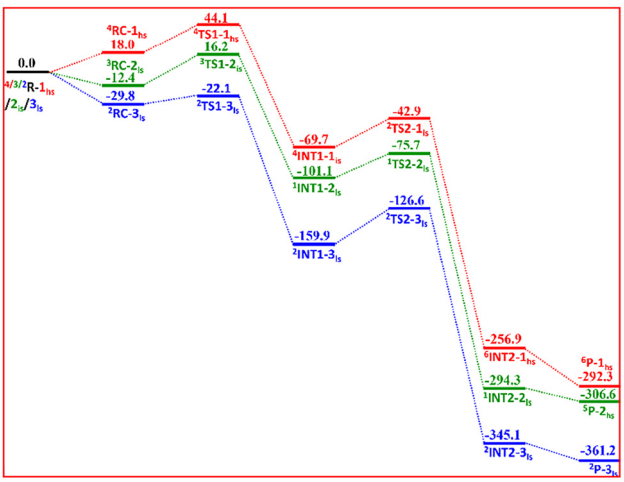

Fig. 5 Computed potential energy (Δ*G* in kJ mol^{-1}) surface of ground states for C–H activation of CHD by **1** (red), **2** (green) and **3** (blue).

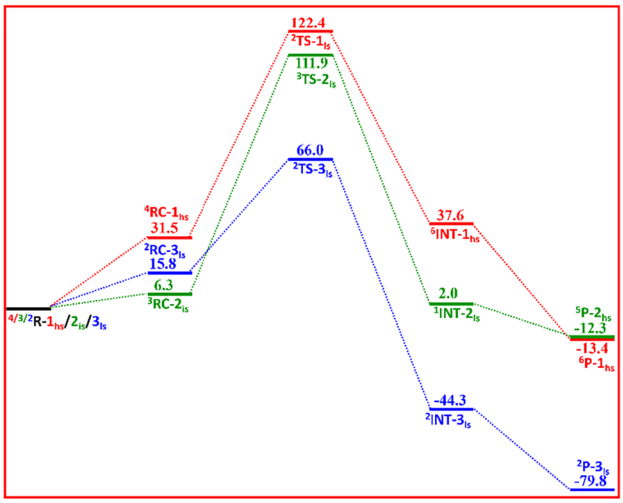

Fig. 6 Computed potential energy (ΔG in kJ mol^{-1}) surface of the ground state for oxidation of SMe_2 by **1** (red), **2** (green) and **3** (blue).

in which the Mn/Fe/Co=O bond is simultaneously cleaved while a new S–O bond is formed. The barrier heights are estimated to be 90.9 kJ mol^{-1} (^{2}**TS-1$_{ls}$**), 105.6 kJ mol^{-1} (^{3}**TS-2$_{is}$**) and 50.2 kJ mol^{-1} (^{2}**RC-3$_{ls}$**) for the species **1**, **2** and **3**, respectively, indicating a kinetically demanding step (see Fig. S10–S12 of the SI).[26c] The Mn/Fe/Co–O bond lengths in the ground states increase, whereas the O–S bond shortens. The bond angle ∠M–O–S is found to be 122.9°/139.4°/129.4° for species **1**/**2**/**3** which depicts the π-pathway during OAT (see Tables S4–S6 of the SI).

The spin density values of 1.69/1.70/0.59 at Mn/Fe/Co centres whereas −0.04/0.19/0.22 and −0.12/0.18/0.16 at the oxygen and sulphur centres, respectively, further support the formation of the O···S bond (see Tables S7–S9 of the SI). Following OAT, the intermediate is formed where the sextet spin state, ^{6}**INT-1$_{hs}$** (37.6 kJ mol^{-1}), is found to be the ground state for species **1**, whereas the singlet, ^{1}**INT-2$_{ls}$** (2.0 kJ mol^{-1}) and doublet, ^{2}**INT-3$_{ls}$** (−44.3 kJ mol^{-1}) were found to be the ground state for species **2** and **3**, respectively, (see Fig. S10–S12 of the SI for other states). In the next step, the final product is formed at −13.4 (^{6}**P-1$_{hs}$**), −12.3 (^{5}**P-2$_{hs}$**) and −79.8 (^{2}**P-3$_{ls}$**) kJ mol^{-1} for species **1**, **2** and **3**, respectively. This pathway is also supported by the previous studies.[56–57,43a] The trend reflected here is similar to that of the C–H activation reaction and suggests that there is a common reactivity trend for these metal–oxo species.

Discussion

Our computed barrier heights reveal that species **3** consistently shows the lowest energy barriers for hydrogen abstraction and oxygen atom transfer across CH_4, CHD and SMe_2 substrates. This persistent barrier reduction establishes species **3** as the most kinetically favorable and catalytically efficient among the three metal–oxo species. The Badger plot also depicts that species **3** possesses the weakest and most activated M–O bond which further supports the computed barriers (see Fig. 2).

To further understand the energetic origins of the HAT and OAT processes, we looked at the deformation energy and interaction energy (see Table S12 of the SI). Transition states associated with the abstraction of hydrogen and transfer of oxygen atoms are computed to evaluate the deformation and interaction energies. In the case of methane activation, the deformation energy values are estimated to be 100.9 (^{4}**TS1-1$_{hs}$**), 101.9 (^{3}**TS1-2$_{is}$**) and 61.1 (^{2}**TS1-3$_{ls}$**) kJ mol^{-1} for **1**, **2** and **3**, respectively. The computed interaction energy significantly contributed to the barrier height in all three species.[41a] For methane activation, the barriers are governed predominantly by deformation energy. In **1**, large deformation energy leads to a higher barrier. In **2** and **3**, a more stabilizing interaction (−16.6 and −27.2 kJ mol^{-1} for ^{3}**TS1-2$_{is}$** and ^{2}**TS1-3$_{ls}$**) lowers the barrier to 85.3 and 33.9 kJ mol^{-1} from the reactant, respectively. These results demonstrate that attractive interaction energy reduces the barrier height. Similarly, in CHD activation, the deformation energies are substantially smaller as compared to methane. The computed deformation energy for **1** is found to be 30.4 kJ mol^{-1} (^{4}**TS1-1$_{hs}$**), whereas for 2 and 3 it is −0.43 kJ mol^{-1} (^{3}**TS1-2$_{is}$**) and −27.8 (^{2}**TS1-3$_{ls}$**) kJ mol^{-1}, respectively. For SMe_2 oxidation, the deformation energy contributes more to the barrier. **1** exhibits a large deformation energy (133.4 kJ mol^{-1} for ^{2}**TS-1$_{ls}$**), whereas **2** displays a more moderate deformation energy (46.5 kJ mol^{-1} for ^{3}**TS-2is**). In **3**, deformation is favourable which leads to a reduced barrier of 66.0 kJ mol^{-1} as compared to **1** and **2**. Overall, these deformation and interaction energy analyses show that lower deformation requirements and increasingly favourable interaction energies from **1** to **3** support the observed reactivity trend.

Furthermore, NCI analysis highlights the role of weak interactions in stabilizing the transition states involved in both the H-atom abstraction and oxygen atom transfer.[58] For all three metal–oxo species reacting with CH_4, CHD and SMe_2, the 3D NCI isosurface consistently displays green regions between the metal–oxo unit and the approaching substrate which is a characteristic of dispersive van der Waals interactions (see Fig. S13–S15 of the SI). These effects are more pronounced for CHD and SMe_2, reflecting their weaker C–H and S–Me bonds and enhanced susceptibility for activation. Collectively, NCI results indicate that these weak interactions support transition state stabilization and correlate well with the observed reactivity trend **3** > **2** > **1**. Steric (%V_{bur}) analysis further clarifies how ligand crowding influences the substrate accessibility.[59,60] All three complexes exhibit buried volumes greater than 86% around the metal–oxo center. These species also show %V_{bur} values in several quadrants particularly in NE and NW regions (see Table S13 and Fig. S16–S19 of the SI). From these computed values it is concluded that all three species have sufficient open space for substrate approach. This suggests that the steric factor alone does not govern reactivity, and electronic factors play a more decisive role.[61]

Furthermore, QTAIM analysis provides additional insights into the electronic structure at the transition states.[62] Species **3**

consistently exhibits lower electron density and less negative total energy density at the M═O bond critical point which shows a more polarized and reactive oxo bond (see Table S14 and Fig. S20–S22 of the SI). In contrast, the O–H and O–S bond critical points formed during HAT and OAT show higher ρ and more negative $H(r)$ values for **3**, indicating a stronger interaction with the substrate. These results also support that **3** possesses a more reactive electronic environment which leads to lower activation barriers. Furthermore, ELF and LOL analyses support this trend by showing increased electron localization and stronger orbital overlap at the metal–oxo and forming bonds in **3**.[63] The transition states involving **3** display more defined ELF and LOL isosurfaces with higher localization values, reflecting more efficient charge reorganizations and stronger directional bonding during HAT/OAT (see Fig. S23–S28 of the SI). Moreover, IRI analysis further differentiates interaction strengths.[64] The transition states involving **3** consistently exhibit denser and more continuous IRI isosurfaces in the O···H–C and O···S interaction regions compared to **1** and **2** (see Fig. S29–S31 of the SI). Overall, all these analyses conclude that **3** exhibits stronger non-covalent stabilization, greater electron localization, more polarized M═O bonds and more favourable orbital interactions than **1** and **2**. These features collectively support the computed reactivity trend **3** > **2** > **1** for both HAT and OAT processes.

Furthermore, the reactivity trends observed in this study align well with the electronic characteristics of Mn/Fe/Co–oxo species reported in the literature.[65] Species **1** is known to be more basic and likely to protonate. This leads to reduced efficiency in C–H activation which results in higher barrier for HAT. On the other hand, **2** has supported concerted HAT mechanisms particularly favoring the activation of weak aliphatic C–H bonds. In contrast, **3** exhibits higher reactivity attributed to its more oxyl character arising from low-lying d-orbitals and greater localization of π* orbitals on the oxygen. These features promote the strong oxyl character at the oxygen center, making **3** highly competent in both HAT and OAT processes.[66,44c]

Furthermore, we also examined how the reaction channel and C–H···π interactions influence the barrier height of the reactions. All three species are found to react through the π-channel, in contrast to non-heme metal–oxo species which typically favor the σ-channel with the substrate to lower the barrier height.[67] To explore the role of secondary interactions in modulating the reactivity, we also examined the presence of CH···π non-covalent interactions in the ground state of transition states for hydrogen atom abstraction by **1–3** (see Fig. 7). These interactions occur between the hydrogen atom of the substrate and the π-electron cloud of the porphyrin ring and are characterized by short H···π distances (2.69–3.65 Å) and favourable ∠CH···π angles (90–130°).[68] This isosurface demonstrates that the π-face of the porphyrin ring and the edge of the substrate group engage in an attractive interaction (see Fig. 7).[69] For CH_4 activation (Fig. 7(a–c)), **3** exhibits a comparatively larger ∠CH···π angle (129.2°) with balanced H···π distances (~2.76 Å), suggesting an optimized geometry for orbital

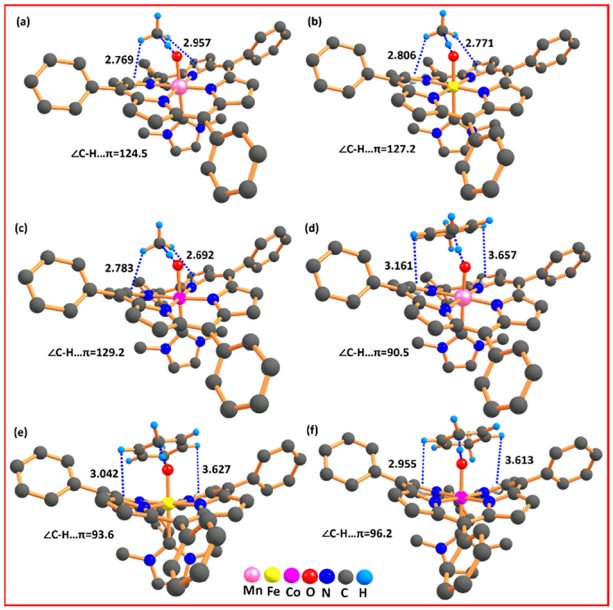

Fig. 7 Optimized structures of the ground state of hydrogen abstraction transition states of CH_4 (a–c) and CHD (d–f) by **1–3** showing the shortest distance between the H atoms of the methyl/MHD group and the π-cloud of the porphyrin ring (CH···π interactions). All the distances are given in Å and angles in°.

alignment during hydrogen atom abstraction. **1** and **2** show slightly bent angles of 124.5° and 127.2°, respectively, but comparable H···π distances (~2.76–2.95 Å). In the case of CHD (Fig. 7(d–f)), the interactions are slightly weaker with longer H···π distances (up to 3.65 Å), yet still within the range of stabilizing noncovalent contacts. These observations collectively support the overall reactivity trend as stronger CH···π stabilization and a more favorable π-channel orientation led to reduced barrier heights in **3** which is also supported by previous studies.[70]

Conclusions

In this study, DFT calculations were employed to understand the electronic structure of high valent heme-based Mn/Fe/Co–oxo species bearing a TPP ligand framework with 1,3-dimethylimidazole as the axial ligand. DFT results affirmed the quartet (^{4}**R-1$_{hs}$**), triplet (^{3}**R-2$_{is}$**) and doublet (^{2}**R-3$_{ls}$**) as the ground states for **1–3**, respectively. In addition to this, the mechanism of C–H bond activation and OAT with substrates CH_4, CHD and SMe by these species has been explored. Across all the substrates examined, the computed barrier heights predicted a reactivity order of **3** > **2** > **1**. Steric map analyses confirmed that all three metal–oxo species provide accessible active sites for substrate approach. Spin density analyses highlighted a significant localization on the terminal oxo group conferring strong oxyl character that enhances catalytic activity. Furthermore, from NCI, QTAIM, deformation–interaction, ELF/LOL and IRI analyses it is concluded that **3** significantly benefitted from enhanced non-covalent stabilization of transition states, stron-

ger polarization of the Co–O bond, greater oxyl radical character and reduced geometric distortion requirements. All of these factors support the higher reactivity of **3**.

To this end, this theoretical study provides a comprehensive mechanistic understanding of how geometric strain, electronic structure and non-covalent interactions collectively influence the reactivity of high-valent metal–oxo complexes. Moreover, these bioinspired model species may serve as promising candidates for advancing the development of improved catalytic systems for selective and efficient C–H and OAT functionalization.

Author contributions

Mukhtar Ahmed: writing – original draft, visualization, validation, methodology, and data curation. Manjeet Kumar: writing – review & editing and formal analysis. Mursaleem Ansari: methodology, data curation, and writing – review & editing. Manoj Kumar Gupta: conceptualization and writing – review & editing. Azaj Ansari: conceptualization, software, supervision, and writing – review & editing.

Conflicts of interest

There are no conflicts to declare.

Data availability

Data details have been included in the supplementary information (SI). Supplementary information is available. See DOI: https://doi.org/10.1039/d5dt03104d.

Acknowledgements

Mukhtar Ahmed would like to thank the HSCSIT for the fellowship. AA would like to thank the Central University of Haryana for providing infrastructural support for this work.

References

1 (*a*) C. Krebs, D.G. Fujimori, C. T. Walsh and J. M. Bollinger, *Acc. Chem. Res.*, 2007, **40**, 484–492; (*b*) M. T. Green, *Curr. Opin. Chem. Biol.*, 2009, **13**, 84–88; (*c*) P. R. O. de Montellano, *Chem. Rev.*, 2010, **110**, 932–948; (*d*) S. Shaik, W. Lai, H. Chen and Y. Wang, *Acc. Chem. Res.*, 2010, **43**, 1154–1165; (*e*) K. Ray, F. F. Pfaff, B. Wang and W. Nam, *J. Am. Chem. Soc.*, 2014, **136**, 13942–13958; (*f*) R. A. Baglia, J. P. T. Zaragoza and D. P. Goldberg, *Chem. Rev.*, 2017, **117**, 13320–13352; (*g*) L. Vicens, G. Olivo and M. Costas, *ACS Catal.*, 2020, **10**, 8611–8631; (*h*) G. Mukherjee, J. K. Satpathy, U. K. Bagha, M. Q. E. Mubarak, C. V. Sastri and S. P. de Visser, *ACS Catal.*, 2021, **11**, 9761–9797.

2 (*a*) J. Rittle and M. T. Green, *Science*, 2010, **330**, 933–937; (*b*) T. A. Betley, Q. Wu, T. Van Voorhis and D. G. Nocera, *Inorg. Chem.*, 2008, **47**, 1849–1861; (*c*) C. W. Cady, R. H. Crabtree and G. W. Brudvig, *Coord. Chem. Rev.*, 2008, **252**, 444–455.

3 (*a*) Y. H. Hong, Y. Jang, R. Ezhov, M. S. Seo, Y. M. Lee, B. Pandey, S. Hong, Y. Pushkar, S. Fukuzumi and W. Nam, *ACS Catal.*, 2021, **11**, 2889–2901; (*b*) H. Kotani, S. Kaida, T. Ishizuka, M. Sakaguchi, T. Ogura, Y. Shiota, K. Yoshizawa and T. Kojima, *Chem. Sci.*, 2015, **6**, 945–955.

4 (*a*) Z. Chen and G. Yin, *Chem. Soc. Rev.*, 2015, **44**, 1083–1100; (*b*) L. V. Liu, S. Hong, J. Cho, W. Nam and E. I. Solomon, *J. Am. Chem. Soc.*, 2013, **135**, 3286–3299.

5 (*a*) G. Mukherjee, C. W. Z. Lee, S. S. Nag, A. Alili, F. G. C. Reinhard, D. Kumar, C. V. Sastri and S. P. de Visser, *Dalton Trans.*, 2018, **47**, 14945–14957; (*b*) S. T. Kleespies, W. N. Oloo, A. Mukherjee and L. Que, *Inorg. Chem.*, 2015, **54**, 5053–5064.

6 (*a*) J. M. Mayer, *Acc. Chem. Res.*, 2011, **44**, 36–46; (*b*) A. S. Borovik, *Chem. Soc. Rev.*, 2011, **40**, 1870–1874; (*c*) A. Gunay and K. H. Theopold, *Chem. Rev.*, 2010, **110**, 1060–1081; (*d*) J. J. Warren, T. A. Tronic and J. M. Mayer, *Chem. Rev.*, 2010, **110**, 6961–7001; (*e*) Monika and A. Ansari, *Dalton Trans.*, 2022, **51**, 5878–5889.

7 (*a*) M. M. Abu-Omar, *Dalton Trans.*, 2011, **40**, 3435–3444; (*b*) P. C. A. Bruijnincx, G. van Koten and R. J. M. K. Gebbink, *Chem. Soc. Rev.*, 2008, **37**, 2716–2744; (*c*) R. van Eldik, *Coord. Chem. Rev.*, 2007, **251**, 1649–1662.

8 (*a*) A. J. Murphy, G. Dubois and D. P. Stack, *J. Am. Chem. Soc.*, 2003, **125**, 5250–5251; (*b*) S. Romain, L. Vigara and A. Llobet, *Acc. Chem. Res.*, 2009, **42**, 1944–1953.

9 (*a*) B. Lassalle-Kaiser, C. Hureau, D. A. Pantazis, Y. Pushkar, R. Guillot, V. K. Yachandra, J. Yano, F. Neese and E. Anxolabéhère-Mallart, *Energy Environ. Sci.*, 2010, **3**, 924–938; (*b*) R. D. Britt, K. A. Campbell, J. M. Peloquin, M. L. Gilchrist, C. P. Aznar, M. M. Dicus, J. H. Robblee and J. Messinger, *Biochim. Biophys. Acta, Bioenerg.*, 2004, **1655**, 158–171; (*c*) X. X. Li, K. B. Cho and W. Nam, *Bull. Korean Chem. Soc.*, 2021, **42**, 1506–1512; (*d*) W. Nam, Y. M. Lee and S. Fukuzumi, *Acc. Chem. Res.*, 2018, **51**, 2014–2022; (*e*) G. Mukherjee, J. K. Satpathy, U. K. Bagha, M. Q. E. Mubarak, C. V. Sastri and S. P. de Visser, *ACS Catal.*, 2021, **11**, 9761–9797.

10 R. Friemann, M. M. Ivkovic-Jensen, D. J. Lessner, C.-L. Yu, D. T. Gibson, R. E. Parales, H. Eklund and S. Ramaswamy, *J. Mol. Biol.*, 2005, **348**, 1139–1151.

11 (*a*) J. P. T. Zaragoza, R. A. Baglia, M. A. Siegler and D. P. Goldberg, *J. Am. Chem. Soc.*, 2015, **137**, 6531–6540; (*b*) A. A. Massie, M. C. Denler, R. Singh, A. Sinha, E. Nordlander and T. A. Jackson, *Chem. – Eur. J.*, 2019, **26**, 900–912; (*c*) M. C. Denler, A. A. Massie, R. Singh, E. Stewart-Jones, A. Sinha, V. W. Day, E. Nordlander and T. A. Jackson, *Dalton Trans.*, 2019, **48**, 5007–5021.

12 (*a*) M. S. Seo, N. H. Kim, K. B. Cho, J. E. So, S. K. Park, M. Clémancey, R. Garcia-Serres, J.-M. Latour, S. Shaik and

W. Nam, *Chem. Sci.*, 2011, **2**, 1039–1045; (*b*) F. P. Guengerich, *ACS Catal.*, 2018, **8**, 10964–10976.
13 R. Gupta, X.-X. Li, Y. Lee, M. S. Seo, Y.-M. Lee, S. Yanagisawa, M. Kubo, R. Sarangi, K.-B. Cho, S. Fukuzumi and W. Nam, *Chem. Sci.*, 2022, **13**, 5707–5717.
14 M. R. Bukowski, K. D. Koehntop, A. Stubna, E. L. Bominaar, J. A. Halfen, M. E. W. Nam and L. Que, *Science*, 2005, **310**, 1000–1002.
15 (*a*) A. R. Groenhof, M. Swart, A. W. Ehlers and K. Lammertsma, *J. Phys. Chem. A*, 2005, **109**, 3411–3417; (*b*) H. Fujii, *J. Am. Chem. Soc.*, 1993, **115**, 4641–4648.
16 (*a*) Y. M. Goh and W. Nam, *Inorg. Chem.*, 1999, **38**, 914–920; (*b*) A. B. Sorokin, *Chem. Rev.*, 2013, **113**, 8152–8191.
17 (*a*) D. Kumar, L. Tahsini, S. P. de Visser, H. Y. Kang, S. J. Kim and W. Nam, *J. Phys. Chem. A*, 2009, **113**, 11713–11722; (*b*) T. Kamachi, T. Kouno, W. Nam and K. Yoshizawa, *J. Inorg. Biochem.*, 2006, **100**, 751–754; (*c*) W. Nam, *Acc. Chem. Res.*, 2007, **40**, 522–531; (*d*) H. Fujii, *Coord. Chem. Rev.*, 2002, **226**, 51–60.
18 (*a*) Z. Ma, N. Nakatani, H. Fujii and M. Hada, *Phys. Chem. Chem. Phys.*, 2020, **22**, 12173–12179; (*b*) Y. Kang, H. Chen, Y. J. Jeong, W. Lai, E. H. Bae, S. Shaik and W. Nam, *Chem. – Eur. J.*, 2009, **15**, 10039–10046; (*c*) D. E. Lansky, A. A. N. Sarjeant and D. P. Goldberg, *Angew. Chem., Int. Ed.*, 2006, **45**, 8214–8217.
19 (*a*) S. Hong, Y.-M. Lee, M. Sankaralingam, A. K. Vardhaman, Y. J. Park, K.-B. Cho, T. Ogura, R. Sarangi, S. Fukuzumi and W. Nam, *J. Am. Chem. Soc.*, 2016, **138**, 8523–8532; (*b*) M. Guo, Y.-M. Lee, R. Gupta, M. S. Seo, T. Ohta, H.-H. Wang, H.-Y. Liu, S. N. Dhuri, R. Sarangi, S. Fukuzumi and W. Nam, *J. Am. Chem. Soc.*, 2017, **139**, 15858–15867.
20 (*a*) D. D. Malik, Y. Lee and W. Nam, *Bull. Korean Chem. Soc.*, 2022, **43**, 1075–1082; (*b*) A. Zhou, X. Cao, H. Chen, D. Sun, Y. Zhao, W. Nam and Y. Wang, *Dalton Trans.*, 2022, **51**, 4317–4323; (*c*) Q. He, M.-P. Pu, Z. Jiang, H. Wang, X. Feng and X. Liu, *J. Am. Chem. Soc.*, 2023, **145**, 15611–15618; (*d*) A. Chandra, M. Ansari, I. Monte-Pérez, S. Kundu, G. Rajaraman and K. Ray, *Angew. Chem., Int. Ed.*, 2021, **60**, 14954–14959.
21 (*a*) Y. Ishimizu, Z. Ma, M. Hada and H. Fujii, *Inorg. Chem.*, 2021, **60**, 17687–17698; (*b*) K. Nishikawa, Y. Honda and H. Fujii, *J. Am. Chem. Soc.*, 2020, **142**, 4980–4984.
22 (*a*) A. Ansari, A. Kaushik and G. Rajaraman, *J. Am. Chem. Soc.*, 2013, **135**, 4235–4249; (*b*) R. Kumar, A. Ansari and G. Rajaraman, *Chem. – Eur. J.*, 2018, **24**, 6818–6827; (*c*) Monika and A. Ansari, *New J. Chem.*, 2020, **44**, 19103–19112.
23 (*a*) A. Sen, N. Vyas, B. Pandey, M. Jaccob and G. Rajaraman, *Isr. J. Chem.*, 2020, **60**, 973–986; (*b*) M. Jaccob, A. Ansari, B. Pandey and G. Rajaraman, *Dalton Trans.*, 2013, **42**, 16518–16526.
24 (*a*) M. Ansari, N. Vyas, A. Ansari and G. Rajaraman, *Dalton Trans.*, 2015, **44**, 15232–15243; (*b*) M. Ansari and G. Rajaraman, *Dalton Trans.*, 2022, **52**, 308–325.
25 A. Hermano, R. Yadav, T. Mokkawes, A. Kumar, M. S. Skaf, C. V. Sastri, D. Kumar and S. P. de Visser, *Inorg. Chem.*, 2023, **62**, 2244–2256.
26 (*a*) S. Meyer, I. Klawitter, S. Demeshko, E. Bill and F. Meyer, *Angew. Chem., Int. Ed.*, 2013, **52**, 901–905; (*b*) M. R. Anneser, S. Haslinger, A. Pöthig, M. Cokoja, V. D'Elia, M. P. Högerl, J.-M. Basset and F. E. Kühn, *Dalton Trans.*, 2016, **45**, 6449–6455; (*c*) F. G. C. Reinhard and S. P. de Visser, *Chem. – Eur. J.*, 2017, **23**, 2935–2944.
27 (*a*) Z. Yao, H. Li, Y. Fan, X. Liang, X. Xu and J. Li, *Dyes Pigm.*, 2020, **173**, 107961; (*b*) Z. Yao, H. Li, X. Liang, X. Xu and J. Li, *Dyes Pigm.*, 2019, **162**, 75–79; (*c*) M. Kumar, M. Ansari and A. Ansari, *Spectrochim. Acta, Part A*, 2023, **284**, 121774; (*d*) X.-X. Li, V. Postils, W. Sun, A. S. Faponle, M. Solà, Y. Wang, W. Nam and S. P. de Visser, *Chem. – Eur. J.*, 2017, **23**, 6406–6418; (*e*) N. Fukui, X.-X. Li, W. Nam, S. Fukuzumi and H. Fujii, *Inorg. Chem.*, 2019, **58**, 8263–8266; (*f*) X. Lu, X.-X. Li, M. S. Seo, Y.-M. Lee, M. Clémancey, P. Maldivi, J.-M. Latour, R. Sarangi, S. Fukuzumi and W. Nam, *J. Am. Chem. Soc.*, 2018, **141**, 80–83; (*g*) L. Zhang, S. R. Premakumari, M. Ng, J. Zhang, Y.-M. Lee, S. Fukuzumi, K.-B. Cho and W. Nam, *Inorg. Chem. Front.*, 2025, **12**, 5730–5740; (*h*) L. Ji, A. S. Faponle, M. G. Quesne, M. A. Sainna, J. Zhang, A. Franke, D. Kumar, R. van Eldik, W. Liu and S. P. de Visser, *Chem. – Eur. J.*, 2015, **21**, 9083–9092; (*i*) M. Oszajca, A. Drzewiecka-Matuszek, A. Franke, D. Rutkowska-Zbik, M. Brindell, M. Witko, G. Stochel and R. van Eldik, *Chem. – Eur. J.*, 2014, **20**, 2328–2343; (*j*) A. Rosa and G. Ricciardi, *Inorg. Chem.*, 2012, **51**, 9833–9845.
28 (*a*) T. R. K. Rana and G. Rajaraman, in *International Workshop on Quantum Systems in Chemistry, Physics, and Biology*, Springer Nature Switzerland, Cham, 2023, pp. 155–175; (*b*) Z. Cong, H. Kinemuchi, T. Kurahashi and H. Fujii, *Inorg. Chem.*, 2014, **53**, 10632–10641; (*c*) L. Tahsini, M. Bagherzadeh, W. Nam and S. P. de Visser, *Inorg. Chem.*, 2009, **48**, 6661–6669; (*d*) D. Balcells, C. Raynaud, R. H. Crabtree and O. Eisenstein, *Chem. Commun.*, 2008, 744–746; (*e*) C. Arunkumar, Y.-M. Lee, J. Y. Lee, S. Fukuzumi and W. Nam, *Chem. – Eur. J.*, 2009, **15**, 11482–11489.
29 M. J. Frisch, G. W. Trucks, H. B. Schlegel, G. E. Scuseria, M. A. Robb, J. R. Cheeseman, G. Scalmani, V. Barone, G. A. Petersson, H. Nakatsuji, X. Li, M. Caricato, A. V. Marenich, J. Bloino, B. G. Janesko, R. Gomperts, B. Mennucci, H. P. Hratchian, J. V. Ortiz, A. F. Izmaylov, J. L. Sonnenberg, D. Williams-Young, F. Ding, F. Lipparini, F. Egidi, J. Goings, B. Peng, A. Petrone, T. Henderson, D. Ranasinghe, V. G. Zakrzewski, J. Gao, N. Rega, G. Zheng, W. Liang, M. Hada, M. Ehara, K. Toyota, R. Fukuda, J. Hasegawa, M. Ishida, T. Nakajima, Y. Honda, O. Kitao, H. Nakai, T. Vreven, K. Throssell, J. A. Montgomery, Jr., J. E. Peralta, F. Ogliaro, M. J. Bearpark, J. J. Heyd, E. N. Brothers, K. N. Kudin, V. N. Staroverov, T. A. Keith, R. Kobayashi, J. Normand, K. Raghavachari, A. P. Rendell, J. C. Burant, S. S. Iyengar, J. Tomasi, M. Cossi,

J. M. Millam, M. Klene, C. Adamo, R. Cammi, J. W. Ochterski, R. L. Martin, K. Morokuma, O. Farkas, J. B. Foresman and D. J. Fox, *Gaussian 16, Revision C.01*, Gaussian, Inc., Wallingford CT, 2016.

30 (*a*) A. D. Becke, *J. Chem. Phys.*, 1993, **98**, 5648–5652; (*b*) S. Grimme, *J. Comput. Chem.*, 2006, **27**, 1787–1799.

31 (*a*) P. J. Hay and W. R. Wadt, *J. Chem. Phys.*, 1985, **82**, 270–283; (*b*) W. R. Wadt and P. J. Hay, *J. Chem. Phys.*, 1985, **82**, 284–298; (*c*) P. J. Hay and W. R. Wadt, *J. Chem. Phys.*, 1985, **82**, 299–310.

32 M. M. Francl, W. J. Pietro, W. J. Hehre, J. S. Binkley, M. S. Gordon, D. J. DeFrees and J. A. Pople, *J. Chem. Phys.*, 1982, **77**, 3654–3665.

33 (*a*) C. Reinhard, A. S. Faponle and S. P. de Visser, *J. Phys. Chem. A*, 2016, **120**, 9805–9814; (*b*) M. Rao, M. Kumar, S. Bhardwaj, A. Sarkar, M. K. Gupta and A. Ansari, *Dalton Trans.*, 2023, **52**, 14160–14169; (*c*) O. Yadav, M. Kumar, R. K. Mohapatra, M. K. Gupta, M. Ansari and A. Ansari, *New J. Chem.*, 2024, **48**, 6132–6141; (*d*) R. Kumar, A. Ansari, P. Comba and G. Rajaraman, *Chem. – Eur. J.*, 2024, **30**, e202303300.

34 M. S. Gordon, D. G. Fedorov, S. R. Pruitt and L. V. Slipchenko, *Chem. Rev.*, 2012, **112**, 632–672.

35 J. Tomasi, B. Mennucci and R. Cammi, *Chem. Rev.*, 2005, **105**, 2999–3094.

36 (*a*) A. Schäfer, H. Horn and R. Ahlrichs, *J. Chem. Phys.*, 1992, **97**, 2571–2577; (*b*) A. Schäfer, C. Huber and R. Ahlrichs, *J. Chem. Phys.*, 1994, **100**, 5829–5835.

37 W. Humphrey, A. Dalke and K. Schulten, VMD: visual molecular dynamics, *J. Mol. Graphics*, 1996, **14**, 33–38.

38 T. Lu, A comprehensive electron wavefunction analysis toolbox for chemists, Multiwfn, *J. Chem. Phys.*, 2024, **161**, 082503.

39 W.-J. van Zeist and F. M. Bickelhaupt, *Org. Biomol. Chem.*, 2010, **8**, 3118–3127.

40 (*a*) R. W. Strozier, P. Caramella and K. N. Houk, *J. Am. Chem. Soc.*, 1979, **101**, 1340–1343; (*b*) D. H. Ess and K. N. Houk, *J. Am. Chem. Soc.*, 2007, **129**, 10646–10647; (*c*) C. Y. Legault, Y. Garcia, C. A. Merlic and K. N. Houk, *J. Am. Chem. Soc.*, 2007, **129**, 12664–12665.

41 (*a*) D. Usharani, D. C. Lacy, A. S. Borovik and S. Shaik, *J. Am. Chem. Soc.*, 2013, **135**, 17090–17104; (*b*) M. Ansari, D. Senthilnathan and G. Rajaraman, *Chem. Sci.*, 2020, **11**, 10669–10687.

42 M. Kumar, M. K. Gupta, M. Ansari and A. Ansari, *Phys. Chem. Chem. Phys.*, 2024, **26**, 4349–4362.

43 (*a*) S. Hong, F. F. Pfaff, E. Kwon, Y. Wang, M.-S. Seo, E. Bill, K. Ray and W. Nam, *Angew. Chem., Int. Ed.*, 2014, **53**, 10403–10407; (*b*) M. K. Goetz, J. E. Schneider, A. S. Filatov, K. A. Jesse and J. S. Anderson, *J. Am. Chem. Soc.*, 2021, **143**, 20849–20862.

44 (*a*) A. P. Ledray, C. M. Krest, T. H. Yosca, K. Mittra and M. T. Green, *J. Am. Chem. Soc.*, 2020, **142**, 20419–20425; (*b*) D. D. Malik, A. Chandra, M. S. Seo, Y.-M. Lee, E. R. Farquhar, S. Mebs, H. Dau, K. Ray and W. Nam, *Dalton Trans.*, 2021, **50**, 11889–11898; (*c*) E. Andris, R. Navrátil, J. Jašík, M. Srnec, M. Rodríguez, M. Costas and J. Roithová, *Angew. Chem., Int. Ed.*, 2019, **58**, 9619–9624.

45 (*a*) T. H. Parsell, M.-Y. Yang and A. S. Borovik, *J. Am. Chem. Soc.*, 2009, **131**, 2762–2763; (*b*) K. Cho, P. Leeladee, A. J. McGown, S. DeBeer and D. P. Goldberg, *J. Am. Chem. Soc.*, 2012, **134**, 7392–7399.

46 (*a*) A. A. Fischer, S. V. Lindeman and A. T. Fiedler, *Dalton Trans.*, 2017, **46**, 13229–13241; (*b*) A. Sen and G. Rajaraman, *Faraday Discuss.*, 2022, **234**, 175–194; (*c*) G. L. Tripodi, J. Yang, Y. Xing, M. S. Seo, Y.-M. Lee, W. Nam and J. Roithová, *J. Am. Chem. Soc.*, 2025, **147**, 45261–45269; (*d*) C. Sun, B. Hu and Z. Liu, *Heteroat. Chem.*, 2012, **23**, 295–303.

47 D. Usharani, D. Janardanan and S. Shaik, *J. Am. Chem. Soc.*, 2011, **133**, 176–179.

48 R. M. Badger, *J. Chem. Phys.*, 1935, **3**, 710–714.

49 (*a*) T. H. Yosca, A. P. Ledray, J. Ngo and M. T. Green, *J. Biol. Inorg. Chem.*, 2017, **22**, 209–220; (*b*) A. Sen, S. Sharma and G. Rajaraman, *Angew. Chem., Int. Ed.*, 2025, **64**, e202419953.

50 (*a*) S. Shaik, D. Kumar, S. P. de Visser, A. Altun and W. Thiel, *Chem. Rev.*, 2005, **105**, 2279–2328; (*b*) S. Shaik, S. Cohen, Y. Wang, H. Chen, D. Kumar and W. Thiel, *Chem. Rev.*, 2010, **110**, 949–1017.

51 A. J. Johansson, M. R. A. Blomberg and P. E. M. Siegbahn, *J. Phys. Chem. C*, 2007, **111**, 12397–12406.

52 (*a*) K.-B. Cho, S. Shaik and W. Nam, *J. Phys. Chem. Lett.*, 2012, **3**, 2851–2856; (*b*) S. Shaik, H. Hirao and D. Kumar, *Acc. Chem. Res.*, 2007, **40**, 532–542; (*c*) R. A. Baglia, M. Dürr, I. Ivanović-Burmazović and D. P. Goldberg, *Inorg. Chem.*, 2014, **53**, 5893–5895; (*d*) X. Wu, M. S. Seo, K. M. Davis, Y. M. Lee, J. Chen, K. B. Cho, Y. N. Pushkar and W. Nam, *J. Am. Chem. Soc.*, 2011, **133**, 20088–20091; (*e*) J. R. Mayfield, E. N. Grotemeyer and T. A. Jackson, *Chem. Commun.*, 2020, **56**, 9238–9255.

53 (*a*) K.-B. Cho, H. Hirao, S. Shaik and W. Nam, *Chem. Soc. Rev.*, 2016, **45**, 1197–1210; (*b*) X. Zhao, Q. Yin, X. Mao, C. Cheng, L. Zhang, L. Wang, T.-F. Liu, Y. Li and Y. Li, *Nat. Commun.*, 2022, **13**, 2721; (*c*) C. Liu, T. de Haas, F. Buda and S. Bonnet, *ACS Catal.*, 2025, **15**, 4681–4697.

54 (*a*) D. Balcells, C. Raynaud, R. H. Crabtree and O. Eisenstein, *Inorg. Chem.*, 2008, **47**, 10090–10099; (*b*) W. Liu and J. T. Groves, *Acc. Chem. Res.*, 2015, **48**, 1727–1735.

55 X. Huang and J. T. Groves, *J. Biol. Inorg. Chem.*, 2017, **22**, 185–207.

56 M. K. Coggins, X.-R. Sun, Y. Kwak, E. I. Solomon, E. V. Rybak-Akimova and J. A. Kovacs, *J. Am. Chem. Soc.*, 2013, **135**, 5631–5640.

57 (*a*) B. Wang, Y.-M. Lee, W.-Y. Tcho, S. Tussupbayev, S.-T. Kim, Y. Kim, M. S. Seo, K.-B. Cho, Y. Dede, B. C. Keegan, T. Ogura, S. H. Kim, T. Ohta, M.-H. Baik, K. Ray, J. Shearer and W. Nam, *Nat. Commun.*, 2017, **8**, 14839; (*b*) A. Sen, N. Vyas, B. Pandey and G. Rajaraman, *Dalton Trans.*, 2020, **49**, 10380–10393; (*c*) J. Yang, H. T. Dong, M. S. Seo, V. A. Larson, Y.-M. Lee, J. Shearer,

N. Lehnert and W. Nam, *J. Am. Chem. Soc.*, 2021, **143**, 16943–16959; (*d*) W. Lai and S. Shaik, *J. Am. Chem. Soc.*, 2011, **133**, 5444–5452; (*e*) D. Kumar, G. N. Sastry and S. P. de Visser, *Chem. – Eur. J.*, 2011, **17**, 6196–6205; (*f*) J. Park, Y. Morimoto, Y.-M. Lee, W. Nam and S. Fukuzumi, *J. Am. Chem. Soc.*, 2011, **133**, 5236–5239; (*g*) K. Ueda, M. Hada and H. Fujii, *Inorg. Chem.*, 2025, **64**, 14940–14951; (*h*) S. Roach, A. S. Faponle, J. K. Satpathy, C. V. Sastri and S. P. de Visser, *J. Chem. Sci.*, 2021, **133**, 61.

58 (*a*) E. R. Johnson, S. Keinan, P. Mori-Sánchez, J. Contreras-García, A. J. Cohen and W. Yang, *J. Am. Chem. Soc.*, 2010, **132**, 6498–6506; (*b*) J. Lei, S. Alessandrini, J. Chen, Y. Zheng, L. Spada, Q. Gou, C. Puzzarini and V. Barone, *Molecules*, 2020, **25**, 4899.

59 C. Duchemin, J. Kim and P. J. Chirik, *JACS Au*, 2023, **3**, 2007–2024.

60 (*a*) A. Poater, B. Cosenza, A. Correa, S. Giudice, F. Ragone, V. Scarano and L. Cavallo, *Eur. J. Inorg. Chem.*, 2009, **2009**, 1759–1766; (*b*) L. Falivene, R. Credendino, A. Poater, A. Petta, L. Serra, R. Oliva, V. Scarano and L. Cavallo, *Organometallics*, 2016, **35**, 2286–2293; (*c*) L. Falivene, Z. Cao, A. Petta, L. Serra, A. Poater, R. Oliva, V. Scarano and L. Cavallo, *Nat. Chem.*, 2019, **11**, 872–879.

61 J. Singh, S. Sharma, A. P. Prakasham, G. Rajaraman and P. Ghosh, *ACS Omega*, 2023, **8**, 21042–21073.

62 E. L. Zins, B. Silvi and M. E. Alikhani, *Phys. Chem. Chem. Phys.*, 2015, **17**, 9258–9281.

63 E. P. Fowe, B. Therrien, G. Süss-Fink and C. Daul, *Inorg. Chem.*, 2008, **47**, 42–48.

64 J. Cai, C. Peng and Y. Wang, *J. Organomet. Chem.*, 2022, **982**, 122534.

65 (*a*) S. C. Sawant, X. Wu, J. Cho, K.-B. Cho, S. H. Kim, M. S. Seo, Y.-M. Lee, M. Kubo, T. Ogura, S. Shaik and W. Nam, *Angew. Chem., Int. Ed.*, 2010, **49**, 8190–8194; (*b*) X.-X. Li, M. Guo, B. Qiu, K.-B. Cho, W. Sun and W. Nam, *Inorg. Chem.*, 2019, **58**, 14842–14852.

66 Y. Shimoyama and T. Kojima, *Inorg. Chem.*, 2019, **58**, 9517–9542.

67 D. Janardanan, Y. Wang, P. Schyman, L. Que, Jr. and S. Shaik, *Angew. Chem., Int. Ed.*, 2010, **49**, 3342–3345.

68 (*a*) O. Takahashi, Y. Kohno and M. Nishio, *Chem. Rev.*, 2010, **110**, 6049–6076; (*b*) D. P. Malenov, G. V. Janjić, D. Ž. Veljković and S. D. Zarić, *Comput. Theor. Chem.*, 2013, **1018**, 59–65; (*c*) Q. Wang, X. Chen, G. Li, Q. Chen, Y.-F. Yang and Y.-B. She, *J. Org. Chem.*, 2019, **84**, 13755–13763.

69 R. S. Proctor, A. C. Colgan and R. J. Phipps, *Nat. Chem.*, 2020, **12**, 990–1004.

70 M. A. Hussain, D. Vijay and G. N. Sastry, *J. Comput. Chem.*, 2016, **37**, 366–377.

